A systematic tomography framework for thickness mapping of pipes using helical guided waves

Zhi Qian[1], Peng Li[1], Zhenghua Qian[1, 2, *], Xianwei Wu[1], Dianzi Liu[3], Iren Kuznetsova[4]

[1] State Key Laboratory of Mechanics and Control for Aerospace Structures, College of Aeronautics, Nanjing University of Aeronautics and Astronautics, Nanjing 210016, China

[2] National Key Laboratory of Helicopter Dynamics, College of Aeronautics, Nanjing University of Aeronautics and Astronautics, Nanjing 210016, China

[3] School of Engineering, University of East Anglia, Norwich NR4 7TJ, UK

[4] Kotel'nikov Institute of Radio Engineering and Electronics of RAS, Moscow 125009, Russia

[*] Corresponding author, **E-mail:** zhenghua_qian@163.com; qianzh@nuaa.edu.cn

Tel.: +86-25-84895952, Fax: +86-25-84891422

Abstract

Pipe wall loss caused by corrosion is of growing interest in the petrochemical industry. A systematic tomography framework using helical guided waves is developed in this paper to conduct a thickness mapping. In this work, the thickness under investigation is reconstructed using an objective function derived from the acoustic Helmholtz equation. The main approach consists of two parts. Firstly, the parametric dictionary is designed to separate the overlapped guided waves travelling in helical paths. After that, the scattering field can be extracted as the input of the distorted born iteration method. The imaging result is exemplified numerically and experimentally, with the strengths and drawbacks explained thoroughly. Remarkably, the thickness error of the simple defect is still within 0.5 mm when the input data is poor. A clear qualitative description of complex defects can be achieved through iterations even in the absence of an initial objective function. The framework established in this paper contributes a comprehensive imaging algorithm and the corresponding signal processing approach, all of which are conducive to providing some reference for engineering applications in nondestructive testing and structural health monitoring.

Keywords: pipe wall, helical guided waves, dictionary reconstruction, thickness mapping.

1. Introduction

Corrosion of pipeline systems presents a notable challenge to the petrochemical industry. Since the long-distance and wide-range inspection feature of ultrasonic guided waves, torsional mode waves emerged as the main focus of non-destructive testing in pipes [1-3]. However, this detection tool is not very accurate. In recent years, research has been conducted on guided wave tomography methods that perform high-precision detection at short distances. This technique mainly employs Lamb wave propagating in helical paths along the pipe, which provides an accurate reconstruction of the wall thickness distribution of pipe sections within a certain range and holds a promising engineering application [4-7].

The axisymmetric torsional mode guided wave T(0,1) [2], propagates parallel to the pipe cross-section, resulting in the simultaneous arrival of direct wave packets received by the array of receivers around the pipe circumference. Unlike this propagation style, infinite propagation paths exist in helical guided waves. The receiving transducer can obtain numerous overlapped wavepackets even with a single mode excitation, making it difficult to be discriminated [5,7]. In order to identify the source and features of the wave packets in the detected signal, much work has been carried out [8-11]. Most of them can only extract the travel time of the wavepacket and distinguish the travelling path. In this case, many tomography methods can not be implemented when precise wavefields are missing. Stylianos [12] separated the full signal with a sparse array arranged in the pipe, while this approach provides poor

imaging resolution. Therefore, a signal processing algorithm that can separate the wave packets is the basic issue that demands to be addressed when performing the tomography method in the pipe. To address it, Huswaite[7] presented a solution to helical path separation for guided wave tomography utilizing a backpropagation technique. Starting from another perspective, this paper utilizes the dictionary to reconstruct the acquired data, realizing the extraction of useful signals, which is a new attempt.

Assuming that the helical guided wave of the single path was obtained, a large amount of previous work could be applied to pipe wall imaging. Among them, the majority of research [13,14] has been concentrated on the inspection of flat plates. Meanwhile, many works [4-7,15] have presented the expansion of the pipe into a plane when dealing with helical guided waves, which means that pipeline tomography can draw on the approach of plates. Several classical algorithms, such as Reconstruction Algorithm for Probabilistic Inspection of Damage (RAPID) [16,17] and Filtered back projection (FBP) [18,19], are highly proficient at calculations. However, they can only determine the locations of defects and exist some misjudgements occasionally. In this paper's background, corrosion causes pipe wall loss. Accurately quantifying the minimum remaining wall thickness is vital to estimating the remaining service life of a pipe and determining whether it can continue to be used safely. The diffraction tomography method based on the Born approximation [20] was adopted early to reconstruct the thickness distribution and gave some experimental validations. Unfortunately, this method demands a reference case with a known depth of flaw.

Building on this work, Hybrid Algorithm for Robust Breast Ultrasound Tomography (HARBUT) [7,21-23] was developed under the same restriction despite significant improvements in imaging resolution. In short, establishing the thickness mapping directly without reference is undoubtedly meaningful. Other methods with great precision are Full Waveform Inversion (FWI) [24-26] and Recursive Extrapolation [27]. The inversion results of FWI are highly sensitive to the initial model, requiring a close approximation to the true medium. If the initial model deviates significantly from the true medium, it may lead to inversion failure or getting stuck in a local optimum. Inaccurate or low-quality data can result in distortion or blurring of the inversion results. The recursive extrapolation algorithm requires an accurate propagation model for image reconstruction. If the propagation model is inaccurate or the assumptions are not valid, the reconstructed results may contain errors.

In our previous works, guided wave tomography based on the method of moment was attempted on the plate [28], and several algorithms have been developed to handle various array structures [29]. Furthermore, pipeline transducer arrays are even more limited in density. It is unknown whether tomographic methods earlier can be applied in practice to pipelines. Therefore, a systematic tomography framework containing signal separation and thickness imaging is proposed to escape the present dilemmas, which is the highlight of this paper. Compared to other signal processing methods, this research is capable of completely separating the signals from different paths, even when they overlap severely. After the separation, the scattering fields can be achieved from the measured signals as input to the imaging algorithm, and then the thickness

reconstruction will be realized without any defect reference using this paper's approach. Firstly, the corresponding method and detailed operations are described in the next section **Theory**. The working performance is examined via the ABAQUS software. Afterwards, experimental measurements are conducted to further verify the tomography framework with the same setting as the simulation. In the discussion section, additional defective forms are simulated to demonstrate both the strengths and drawbacks of this approach. Additionally, comparisons with the former algorithm are presented here. The proposed framework is expected to offer valuable guidance for structural health monitoring in the pipe industry.

2. Theory

The main research of this paper is to achieve a quantitative description of surface defects on pipe walls using helical guided waves. The pipe, as a hollow cylindrical structure, is continuous in the circumferential direction. When the helical Lamb wave was generated at a certain point, it will cause an omnidirectional wave field propagating along the pipe wall, as is shown in Fig.1. A forward model describing the interaction between helical guided waves and defects has been developed in this paper based on the method of moments and the corresponding solution algorithm is provided to perform the inversion. The specific operation program can be seen as follows.

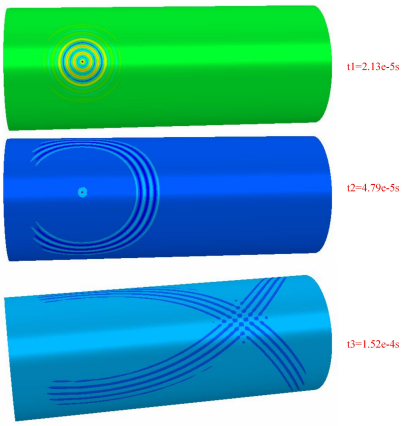

Fig.1. A schematic diagram of the helical Lamb wave propagation process in the pipe wall. It was drawn from the stress distribution at three moments using an Abaqus simulation.

2.1 Forward model

The excitation and reception arrays are necessary to arrange around the detection area when using tomographic techniques. The basic form is illustrated in Fig.2(a). The pipe wall can be approximated as a planar model if the pipe thickness is less than around 10% of the radius [4-7,15,30-32], which is the case for the majority of pipes of interest. In this case, Lamb wave propagation satisfies the Rayleigh-Lamb secular equation [33]. Based on this, the relationship between phase velocity and wall thickness can be established. In contrast to the plane, there are infinite helical propagation paths between each source and receiver pair. Multiple replications of the surface κ could be considered in Fig.2(b) ($\kappa = -\infty, ..., -2, -1, 0, 1, 2, ..., +\infty$). Correspondingly, the expanded wall can be called …,*Order -2*, *Order -1*, *Order 0*, *Order 1*, …, $+\infty$.

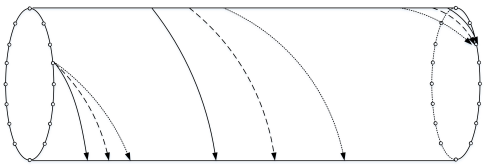

(a)

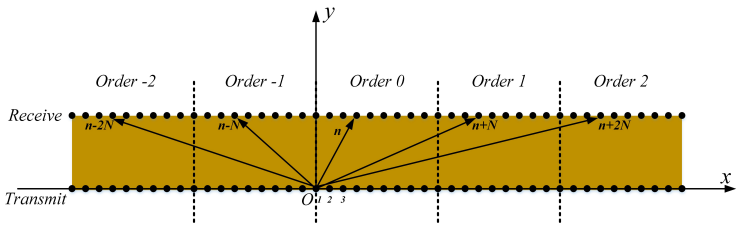

(b)

Fig.2. (a) The basic form of the pipe array structure and the wave propagation of partial helical guided waves. (b)The schematic diagram of pipe wall expansion. Take *Order m* as the list of wall planes after expansion. The probe number is named by *n*, and the number of probes for both excitation and reception arrays is *N*.

Follow naming rules of the serial number in Fig.2(b). The helical Lamb wave emitted from the source will be received infinite times at the *n*-th probe. The serial number of the *n*-th receiving probe in the *Order m* plane is denoted as *n*+*mN*. Select the first excitation probe on the *Order 0* plane as the zero point to establish the Cartesian coordinate system. The travelling path between the *p*-th excitation probe and the (*n*+*mN*)-th receiving probe is recorded as $l(p,n+mN)$, the length expression is:

$$\left|l(p,n+mN)\right|=\sqrt{(x_{n+mN}-x_p)^2+D^2} \tag{1}$$

In which: x_{n+mN} is the abscissa of the (*n*+*mN*)-th receiving probe, x_p is the abscissa of the *p*-th excitation probe, and *D* represents the axial length of the pipe inspection. On the basis of plane expansion and straight ray assumption, the

propagation and scattering of the helical Lamb wave in pipes can be described through the inhomogeneous Helmholtz equation [34-35]:

$$[\nabla^2 + k_0(\omega)^2]\boldsymbol{U}(\boldsymbol{r},\omega) = -k_0(\omega)^2[c_0(\omega)^2 / c^2(\boldsymbol{r},\omega) - 1]\boldsymbol{U}(\boldsymbol{r},\omega) \tag{2}$$

Here: ω is the angular frequency, $\boldsymbol{r}$ is the spatial position of a point in the detection area, $\boldsymbol{U}(\boldsymbol{r},\omega)$ is the potential function of the displacement, $k_0(\omega)$ and $c_0(\omega)$ represent the wavenumber and phase velocity of helical Lamb wave in the defectless pipe wall, respectively. $c(\boldsymbol{r},\omega)$ is the actual phase velocity at the point $\boldsymbol{r}$. When the frequency is fixed, $\boldsymbol{U}(\boldsymbol{r},\omega)$ and $c(\boldsymbol{r},\omega)$ can be simplified as $\boldsymbol{U}(\boldsymbol{r})$ and $c(\boldsymbol{r})$. As displayed in Fig.3, $\boldsymbol{r}_1$ and $\boldsymbol{r}_2$ represent the excitation and receiving point, respectively.

Let $O(\boldsymbol{r}) = k_0{}^2\left\{[c_0 / c(\boldsymbol{r})]^2 - 1\right\}$, Eq.(2) here can be written to:

$$\boldsymbol{U}(\boldsymbol{r}) = \boldsymbol{U}_u(\boldsymbol{r}) + \boldsymbol{U}_s(\boldsymbol{r}) \tag{3}$$

$$(\nabla^2 + k_0{}^2)\boldsymbol{U}_u(\boldsymbol{r}) = 0 \tag{4}$$

$$(\nabla^2 + k_0{}^2)\boldsymbol{U}_s(\boldsymbol{r}) = -O(\boldsymbol{r})\boldsymbol{U}(\boldsymbol{r}) \tag{5}$$

In which: $\boldsymbol{U}(\boldsymbol{r}), \boldsymbol{U}_u(\boldsymbol{r}), \boldsymbol{U}_s(\boldsymbol{r})$ are the total field, incident field and scattering field respectively. And the Green's function G_u is the solution to $(\nabla^2 + k_0{}^2)G_u = \delta$. Therefore, Green's function can be viewed as the scattering field of a point source. If we consider the scattering region as an array of scattering points, then the scattering field can be represented as the superposition of scattering from these point sources, namely:

$$\boldsymbol{U}_s(\boldsymbol{r}_2) = -\int G(\boldsymbol{r} - \boldsymbol{r}_2)O(\boldsymbol{r})\boldsymbol{U}(\boldsymbol{r})d\boldsymbol{r} \tag{6}$$

Therefore, the solution of Eq.(2) can be written as [34]:

$$\boldsymbol{U}(\boldsymbol{r}_2)=\boldsymbol{U}_u(\boldsymbol{r}_2)+\boldsymbol{U}_s(\boldsymbol{r}_2)=\boldsymbol{U}_u(\boldsymbol{r}_2)-\int G(\boldsymbol{r}-\boldsymbol{r}_2)O(\boldsymbol{r})\boldsymbol{U}(\boldsymbol{r})d\boldsymbol{r} \tag{7}$$

Here, $G(\boldsymbol{r}-\boldsymbol{r}_2)=-j/4\cdot H_0^{(2)}(k_0|\boldsymbol{r}-\boldsymbol{r}_2|)$ is the Green's function, and j is the imaginary unit. $H_p^{(q)}(x)$ represents p-th order Hankel function of class q. $O(\boldsymbol{r})$ is the objective function. In general, $\boldsymbol{U}_u(\boldsymbol{r}_2)$ can be calculated by the Green's function.

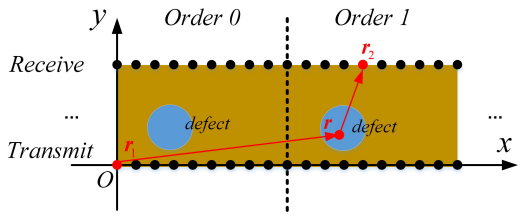

Fig.3. The diagram of the scattering on the pipe wall.

In order to facilitate the calculation, the pipe wall shown in Fig.3 can be divided into grids. Assuming that the number of grids is I, Eq.(7) can be rewritten in the form of an algebraic summation based on the method of moments.

$$\boldsymbol{U}(\boldsymbol{r}_{i_1})=\boldsymbol{U}_u(\boldsymbol{r}_{i_1})+\boldsymbol{U}_s(\boldsymbol{r}_{i_1})=\boldsymbol{U}_u(\boldsymbol{r}_{i_1})+\sum_I O(\boldsymbol{r}_{i_2})\boldsymbol{U}(\boldsymbol{r}_{i_2})c_{i_1i_2} \tag{8}$$

In which:

$$c_{i_1i_2}=\begin{cases} j/2\cdot[\pi k_0 a H_1^{(2)}(k_0a)-2j] & ,i_1=i_2; \\ j/2\cdot\pi k_0 a\cdot J_1(k_0a)H_0^{(2)}(k_0R_{i_1i_2}) & ,\ i_1\neq i_2. \end{cases} \tag{9}$$

Here $i_1,i_2=1,2,3,...,I$ represent the serial number of grid points, located at the center of the grid. a is the radius of the grid and $R_{i_1i_2}$ is the distance between i_1 and i_2. $J_1(x)$ stands for the first order Bessel function. In this condition, $\boldsymbol{U}_s(\boldsymbol{r}_{i_1})=\sum_I O(\boldsymbol{r}_{i_2})\boldsymbol{U}(\boldsymbol{r}_{i_2})c_{i_1i_2}$. Record the receiving probe number as i_3 ($i_3=n+mN$), when the grid point i_1 coincides with the receiving probe i_3, the scattering field can be expressed as:

$$\boldsymbol{U}_s(\boldsymbol{r}_{i_3}) = \sum_I O(\boldsymbol{r}_{i_2})\boldsymbol{U}(\boldsymbol{r}_{i_2})d_{i_3 i_2} \tag{10}$$

$d_{i_3 i_2}$ is the special form of $c_{i_1 i_2}$ with the same expression, Eqs. (6) and (7) can be rewritten into the form of the matrix:

$$\boldsymbol{U}^{(t)} = \boldsymbol{U}^{(in)} + \boldsymbol{COU}^{(t)} \tag{11}$$

$$\boldsymbol{U}^{(s)} = \boldsymbol{DOU}^{(t)} \tag{12}$$

Where: $\boldsymbol{U}^{(t)}$, $\boldsymbol{U}^{(in)}$ and $\boldsymbol{U}^{(s)}$ stand for the matrix of the total field, incident field and scattering field, respectively. The composition of $\boldsymbol{C}$ and $\boldsymbol{D}$ take $c_{i_1 i_2}$ and $d_{i_3 i_2}$ as the basic element. $\boldsymbol{O}$ represent the objective function. Eqs. (11) and (12) are the final forward governing equations, based on which the following inversions will be carried out.

2.2 The technique of dictionary reconstruction

The forward model of helical guided waves travelling in the pipe wall has been given in section 2.1. The forward input of Eq.(12) is the scattering field $\boldsymbol{U}^{(s)}$, which can be achieved from simulation or experiment. However, the helical Lamb mode wave packets will be overlapped due to the multimodes and multipaths when measuring the helical guided waves. How to extract the single mode wave in a specific path plays a key role in solving the problem. In the case of low frequency-thickness products, there are only A0 and S0 modes. The group velocities of these two helical Lamb modes are widely different, which can be easily obtained from the dispersion curve. Therefore, the single mode helical Lamb wave could be extracted based on propagation velocity. As is displayed in Fig.4(a), the *n*-th and (*n*+*N*)-th probes are the same receivers that can

acquire signals from both S1 and S2 paths. However, the propagation distances between the two paths are close, Fig.4 (b) shows the overlapping situation in the time domain. For the purpose of solving the dilemma, an overcomplete path dictionary has been established to extract the time-domain signals from the single mode.

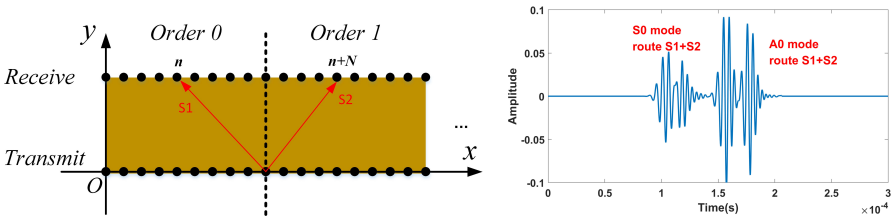

(a) (b)

Fig.4.(a) The schematic diagram for the propagation of two specific signal paths, S1 and S2 are close in length. (b) The actual received signal containing two propagations with A0 and S0 modes.

This technique mainly relies on the dispersion curves of Lamb waves propagating through the plate. At high frequencies, the properties of helical Lamb waves are similar to those of flat plates. In this paper, it is necessary to thoroughly consider the comparison between helical Lamb waves and flat plates under low frequency-thickness products. As shown in Fig.5(a), $c(\boldsymbol{r},\theta)$ is phase velocity with θ being the angle formed by the propagation direction and the x-axis. $c_x(\boldsymbol{r})$ and $c_y(\boldsymbol{r})$ are the circumferential and axial propagation phase velocities of the pipe, where $c_y(\boldsymbol{r})$ can be considered equivalent to propagation in a flat plate. The expression for $c(\boldsymbol{r},\theta)$ can be written as [15]:

$$c(\boldsymbol{r},\theta)=\frac{c_x(\boldsymbol{r})c_y(\boldsymbol{r})}{\sqrt{c_x(\boldsymbol{r})^2\sin^2\theta+c_y(\boldsymbol{r})^2\cos^2\theta}} \tag{13}$$

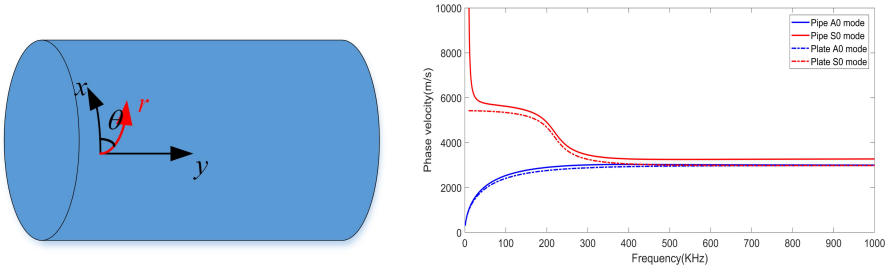

(a) (b)

Fig.5. The pipeline coordinate system and the dispersion curve. (a). Coordinate system of the pipeline structure. (b) The circumferential dispersion curve of the pipeline and the dispersion curve of the flat plate at low frequency-thickness products.

Fig.5(b) shows the dispersion curves for two Lamb wave modes in both a steel pipe (outer diameter is 219mm, thickness is 10.95mm) and a flat plate (thickness is 10.95mm). Based on Fig.5 and Eq.(13), for the selected pipe diameter and thickness, an analysis of the error between the phase velocity of helical and traditional Lamb waves displayed in Fig.6(a) reveals that the error in the circumferential Lamb wave velocity along the pipe is the largest, at around 5%. With a wall thickness of 10.95mm, equivalent to 10% of the pipe radius, we consider the circumferential Lamb wave with the maximum error as an example. The comparison of errors between helical Lamb waves and plate Lamb waves is illustrated in Fig.6(b), covering a wall thickness-to-pipe radius ratio ranging from 5% to 10%. This indicates that at lower frequencies, thinner pipe walls result in higher accuracy of helical Lamb waves. When determining

the frequency and thickness of helical Lamb waves, they can be treated as flat plate waves within a reasonable margin of error.

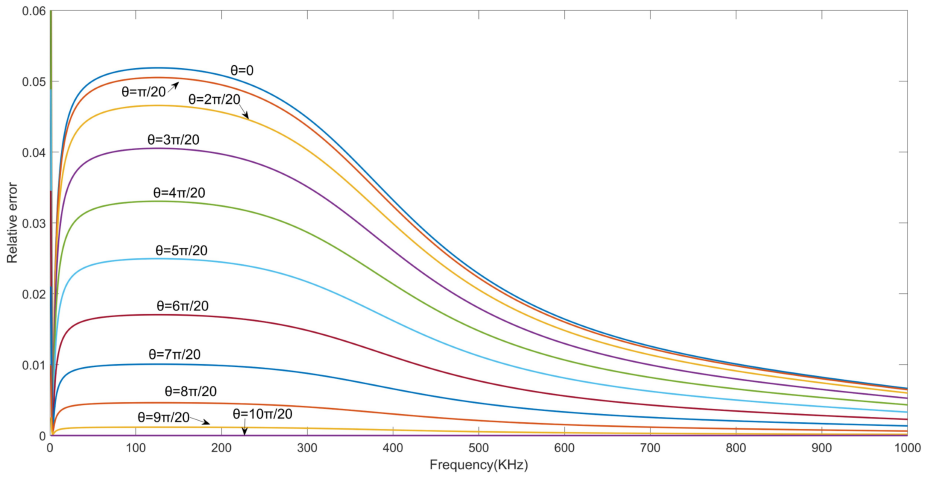

(a)

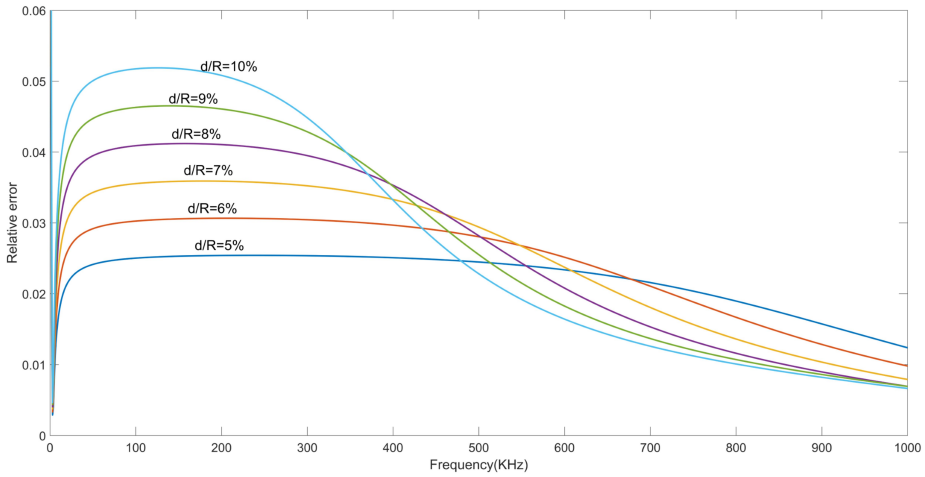

(b)

Fig.6. Error analysis of pipeline dispersion curves caused by different angles and wall thicknesses. (a) At d/R = 10%, the relative error analysis of helical Lamb waves compared to plate Lamb waves for different propagation directions. d is the wall thickness and R is the pipe radius; (b). The analysis of errors between circumferential Lamb waves in the pipeline and plate Lamb waves when the range of d/R varies from

5% to 10%.

When the dispersion relationship of helical Lamb waves is established, the specific wavefield separation techniques are as follows and more detailed derivation steps can be referred to [36].

Select a windowed cosine function $f(t) = w(t)\cos(\omega t)$ as the excitation of the guided wave, $w(t)$ is the windowed function, ω is the angular frequency, t represents the time item. When the excitation propagates at a distance of *x*, a linear mapping technique for dispersion removal of Lame waves [9,37-38] can be utilized to obtain the response of signal:

$$f(x,t) = A \cdot w(t - k_1 x)\cos(\omega_0 t - k_0 x) \tag{14}$$

In which $k_0 = \omega_0 / c_p(\omega_0)$, $k_1 = 1/c_g(\omega_0)$, $c_p(\omega_0)$ and $c_g(\omega_0)$ are the phase velocity and group velocity at the central frequency ω_0. Let $t_1 = k_1 x$, it represents the propagation time when the signal travelled at a distance of *x*. $f(x,t)$ can be replaced by:

$$f(t_1,t) = A \cdot w(t - t_1)\cos[\omega_0(t - t_1) + \omega_0 t_1 - k_0 / k_1 \cdot t_1] \tag{15}$$

Here: A means the amplitude. Let $\varphi = \omega_0 t_1 - k_0 / k_1 \cdot t_1$, it represents the phase variation. Assuming that the signal received by the transducer contains multiple paths, an overcomplete path dictionary $\boldsymbol{L} = [\boldsymbol{L}_1, \boldsymbol{L}_2, ..., \boldsymbol{L}_r, ..., \boldsymbol{L}_R]$ can be built for these path elements. In which: $r = 1, 2, 3, ..., R$, $\boldsymbol{L}_r$ represents the *r*-th path. Since various pipe wall boundary conditions will cause a phase shift of the signal in each path, a phase dictionary $\boldsymbol{\phi} = [\boldsymbol{\phi}_1, \boldsymbol{\phi}_2, ..., \boldsymbol{\phi}_s, ..., \boldsymbol{\phi}_S]$ can be constructed for each path dictionary.

$s = 1, 2, 3, ..., S$ stands for the marks of phase.

Based on the planar expansion technique given in section 2.1, all the propagation paths can be predetermined for each receiving signal. Taking the A0 mode signal in Fig.4(b) as an example, it contains two paths in total. At this point *R*=2, each data set of the path is divided into *S* phases. The original signal can be processed into a single mode by adding a windowed function, this single mode signal is denoted as $\boldsymbol{y}$. It can be written in the form of $\boldsymbol{y} = \boldsymbol{L}\boldsymbol{x} + \boldsymbol{e}$ with the help of path dictionary. Assuming that the signal $\boldsymbol{y}$ contains Y time items, then the dimension of $\boldsymbol{y}$ is $Y \times 1$. On this basis, the dimension of $\boldsymbol{L} = [\boldsymbol{L}_1, \boldsymbol{L}_2, ..., \boldsymbol{L}_r, ..., \boldsymbol{L}_R]$ is $Y \times (R \cdot S)$. $\boldsymbol{x} = \begin{bmatrix} \boldsymbol{x}_1 \\ \boldsymbol{x}_2 \\ \cdots \\ \boldsymbol{x}_r \\ \cdots \\ \boldsymbol{x}_R \end{bmatrix}$ is the weighting factor of the multipath, and its dimension is $(R \cdot S) \times 1$, $\boldsymbol{e}$ is the error item. The so-called separating algorithm is to solve the optimization problem $\min \left\| \boldsymbol{y} - \boldsymbol{L}\boldsymbol{x} \right\|_2^2$. After obtaining $\boldsymbol{x}$, $\boldsymbol{y}_r = \boldsymbol{L}_r \cdot \boldsymbol{x}_r$ can be calculated to achieve the single path signal.

2.3 Inverse model

In section 2.1, the forward governing Eq.(11) and (12) have been deduced. The objective function $\boldsymbol{O}$ is the component to be solved and the scattering field $\boldsymbol{U}^{(s)}$ is the input. Section 2.2 describes the method for extracting the single helical Lamb wavefield. As a matter of course, if the signals do not overlap, it can truncate the signals directly to reduce the computational effort. The specific scattering field is obtained by

measuring the subtraction between the defective signal and the defectless signal in the frequency domain. If there is no healthy signal available as a reference, the Green's function can be directly computed to replace the incident field. Up to now, the extraction of the experimental scattering field [20-23] still relies on subtracting signals to obtain it.

The following is the procedure for solving the objective function.

Firstly, $\boldsymbol{U}^{(s)}$ can be achieved from simulation or experiment. On the basis of Born approximation, $\boldsymbol{U}^{(t)} = \boldsymbol{U}^{(in)}$, Eq.(12) can be replaced by $\boldsymbol{U}^{(s)} = \boldsymbol{DOU}^{(in)}$ and $\boldsymbol{U}^{(in)}$ will be calculated by Green's function. Then, the initial objective function $\boldsymbol{O}_0$ could be obtained. This result is not accurate enough and needs more iterations. The number of iterations can be denoted by k (k=1,2,3,…), substitute $\boldsymbol{O}_{k-1}$ into Eq. (11) to solve the full field $\boldsymbol{U}_k^{(t)}$. At the same time, $\boldsymbol{D}_k$ should be modified by $\boldsymbol{D}_k = \boldsymbol{D}_{k-1}(\boldsymbol{I} - \boldsymbol{O}_{k-1}\boldsymbol{C})^{-1}$. Calculate the difference between the latest scattering field and the measured scattering field $\Delta\boldsymbol{U}_k^{(s)} = \boldsymbol{U}_k^{(s)} - \boldsymbol{U}^{(s)}$. Afterwards, $\Delta\boldsymbol{O}_k$ can be solved from $\Delta\boldsymbol{U}_k^{(s)} = \boldsymbol{D}_k\Delta\boldsymbol{O}_k\boldsymbol{U}_k^{(t)}$. Let $\boldsymbol{O}_k = \boldsymbol{O}_{k-1} + \Delta\boldsymbol{O}_k$ and start the next iteration. Finally, when the error $\Delta\boldsymbol{U}_k^{(s)}$ reaches a certain accuracy δ, the iteration is stopped. The above solution algorithm is the basic idea of the distorted born iteration method [39,40].

When the final objective function is achieved, $c(\boldsymbol{r}) = k_0 c_0(\boldsymbol{r}) / \sqrt{O(\boldsymbol{r}) + k_0^{\,2}}$ can be calculated by $O(\boldsymbol{r}) = k_0^{\,2}\left\{[c_0 / c(\boldsymbol{r})]^2 - 1\right\}$. $c(\boldsymbol{r})$ is the phase velocity at the detection point $\boldsymbol{r}$. It can be converted to the thickness distribution based on the dispersion curve. The ultimate purpose of this paper is to measure the corrosion of the pipe wall utilizing the thickness distribution. The procedure of the proposed method is

shown in Fig.7.

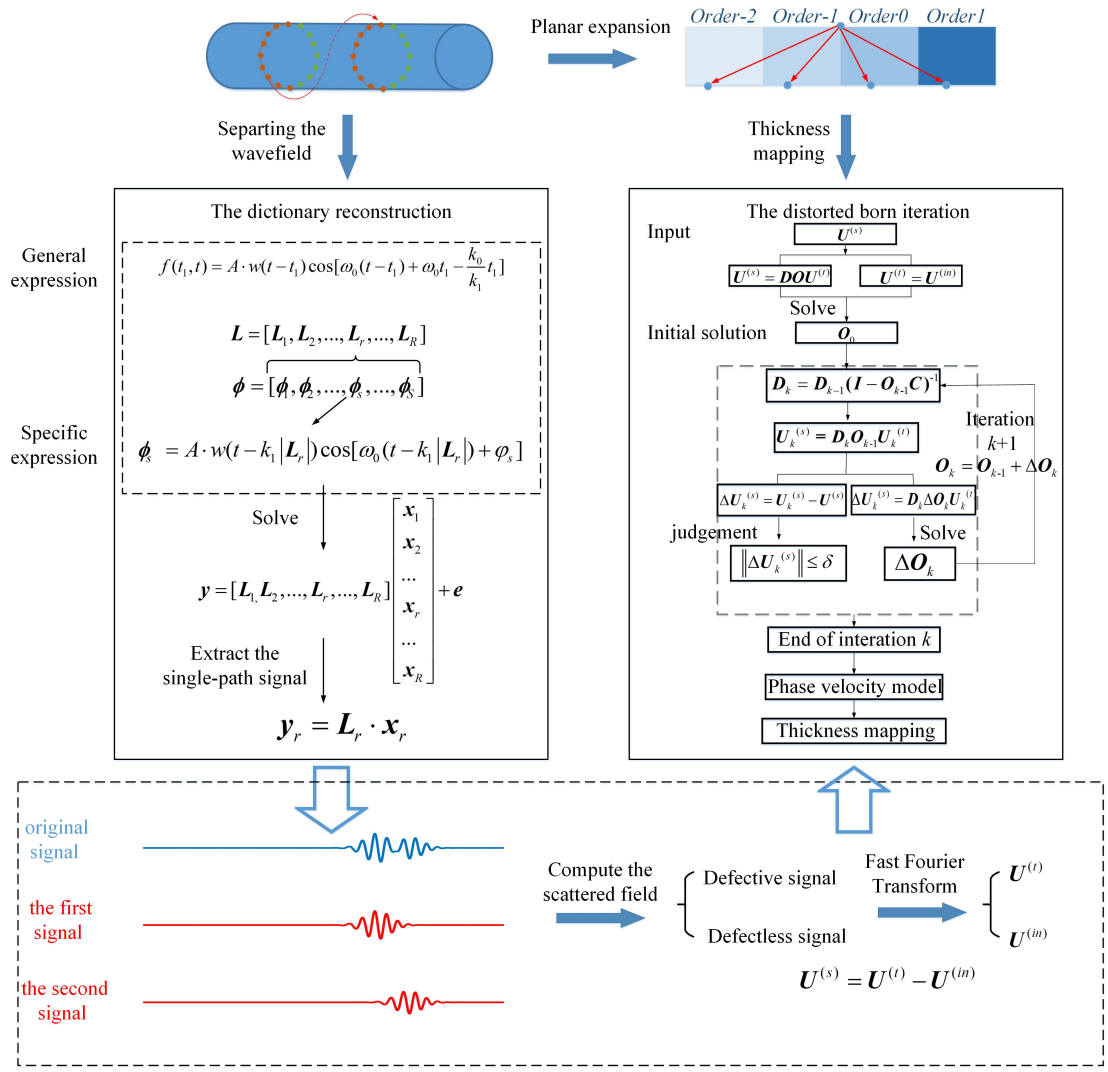

Fig.7. Schematic of the algorithm, containing the signal separation and the imaging method.

3. Numerical model

3.1 Simulated setup

In order to verify the imaging theory, a pipe model was established using ABAQUS software. As displayed in Fig.8, the same amount of transducer arrays are arranged on both sides of the detection area and each array is equipped with 16 probes.

The length of the detection area is 30cm, with a pipe diameter of 219mm and a wall thickness of 6mm. In this pipe condition, the dispersion relationship error of Lamb waves in the pipe wall and flat plate is within 3%. The material is iron (Young's modulus = 210 Gpa, Poisson ratio = 0.3, density = 7850 kg/m^3). The relative single A0 mode wavefield was excited at a point in the ring array, perpendicular to the outer surface and then the other array with all probes would capture the transmission signal. Absorbing boundaries of 40 layers were modelled at the end of the pipeline utilizing the increased damping to avoid reflections [41-43]. The excitation signal is a five-peaked wave expressed in Eq. (16).

$$f(t)=[1-\cos(2\pi f_0 t/5)]\cdot\cos(2\pi f_0 t) \tag{16}$$

Here, $f_0=200\text{kHz}$ is the centre frequency. Cubic elements with an approximate size of 1mm have been utilized to discretize the pipe model into 3618073 nodes. There are 5000 incremental steps set in the model and each step is 1e-7s. The average computation time per incremental step is 0.7145s when using a common computer with 11th Gen Intel Core i7-11700 @ 2.50 GHz. As required by the array, it is necessary to repeat the calculation 16 times, taking a total time of about 15.88 hours.

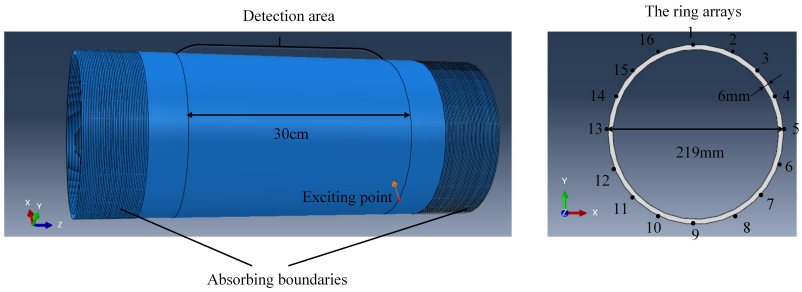

Fig.8. Simulated setup for capturing the helical-guided waves in an iron pipe.

3.2 The imaging results

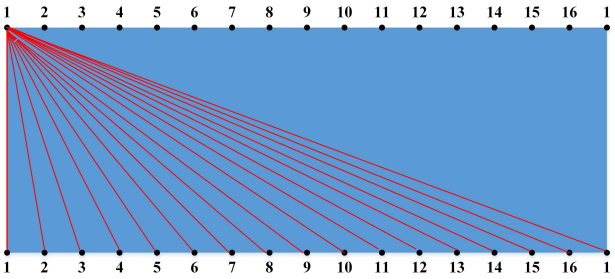

Fig.9. The partial propagation routes of the helical guided wave travelling in the pipe wall of *Order 0*, with a total of 17×17 sets of data available.

As set in the simulation, each array is equipped with 16 probes. On this basis, the ultimate scattered field can be obtained in 289 groups (Fig.9) by considering only the helical guided wave in the pipe wall of *Order 0*. In the forward part of the imaging algorithm, the detection area is evenly divided into 3306 grids. Obviously, the input data would be insufficient. In order to improve the imaging resolution, the received signals travelling through the pipe walls of *Order 0* and *Order -1* are considered, then a total of 1089 sets of scattered fields can be achieved. When the objective function is transformed into a thickness distribution, the imaging results are shown in Fig.10. The defect is a flat circular shape with a diameter of 6cm.

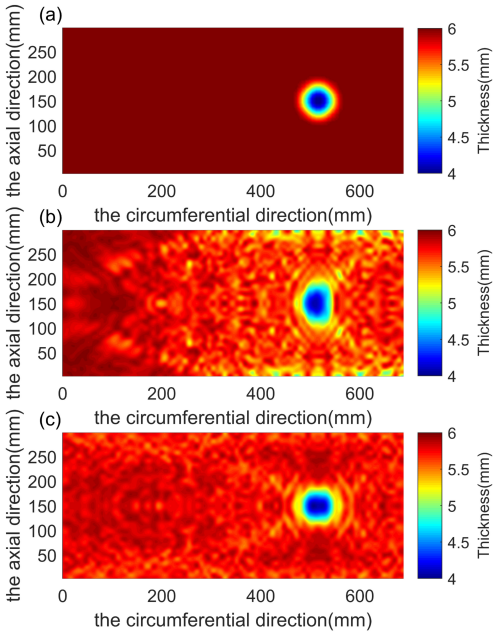

Fig.10. Thickness distribution of the pipe wall. (a) The theoretical thickness distribution; (b) The thickness imaging only considering the direct paths; (c) The thickness imaging considering the direct and helical paths.

Based on the deepest point of defect in the imaging area, the accuracy analysis of the detection results is shown in Table 1. It can be noticed that the remaining thickness and location of the defects are well reconstructed. When the high-order helical guided waves are considered, the thickness error is controlled within 3% and this is very accurate. Reconstruction results only relying on the direct waves have a large error. It can also be visualized from Figs. 10(b) and 10(c) that when the input scattering field of the imaging algorithm is insufficient, the noise pollution of the imaging results is more severe. If the number of probes is certain, the imaging accuracy can be significantly improved by making full use of the propagation characteristics of helical guided waves. In order to better verify the algorithm, an experimental platform is built in this paper

with the same setting conditions in the next section.

Table 1

The accuracy analysis of the detection results.

	Defect location (mm)	Location error (mm)	Defect remaining thickness (mm)	Thickness error (%)
Fig.10(a)	(516,150)	/	4	/
Fig.10(b)	(508,148)	8.246	4.264	6.6%
Fig.10(c)	(510,149)	6.083	4.102	2.55%

4. Experimental verification

4.1 Experimental setup

A stretch of pipe with the same dimensions as the simulation was selected for experimental verification. In order to provide the same defects as the simulation, a 3D-printed mould was fabricated and adhered to the surface of the pipe using epoxy glue. Then hydrochloric acid (20%) was poured into the mould. After 1 month of continuous soaking, the remaining thickness of the pipe became 4mm. The defects generated by this method can be approximately considered as flat. The excitation array consists of 16 circular plain piezoelectric transducers and the receiving array uses commercial transducers (HS-GP) with a centre frequency of 200 kHz to enhance the signal-to-noise ratio. Both of these transducers have a diameter of 1cm. The guided wave detection system (Fig.11) is composed of a signal generator (DG-4102), a power amplifier

(Aigtek-2022H), a pipe containing the corrosion defect, an oscilloscope (MDO-3204) and a computer with the control software. During the experiment, the pipe was placed directly upright on the ground. The total length of the pipe is 1.5m, and within the limited acquisition range, there are no reflected waves.

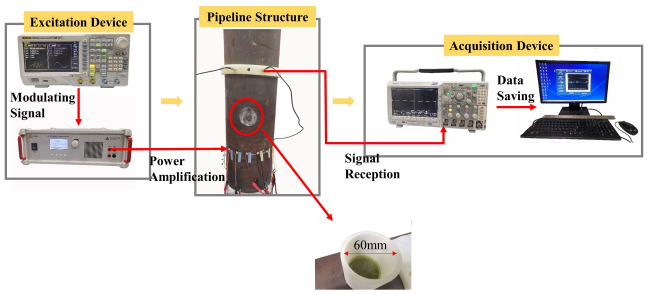

Fig.11. Experimental testing platform.

4.2 Signal processing for experiments

Compared with the simulated signal, the experimental acquisition data contain much noise. Moreover, the signal excited by the piezoelectric transducer also contains the S0 mode, which further enhances the challenge of signal processing. As illustrated in Fig.12(a), the helical guided wave Γ_α can be generated from the transmitter T_q to the receiver R_p, in which $\alpha = \dfrac{p-q-(n_2-n_1)}{N}$, n_1 and n_2 are the serial numbers for the excitation and receiving probe arranged in the pipe wall of *Order 0*, respectively. Taking the received signal shown in Fig.12(b) as an example, the signal consists of A0 and S0 modes, but the S0 mode has a low amplitude and may be drowned in the vibration noise during propagation. Therefore, we only consider the propagation of the A0 mode in this paper, and the specific processing is shown in Fig.13.

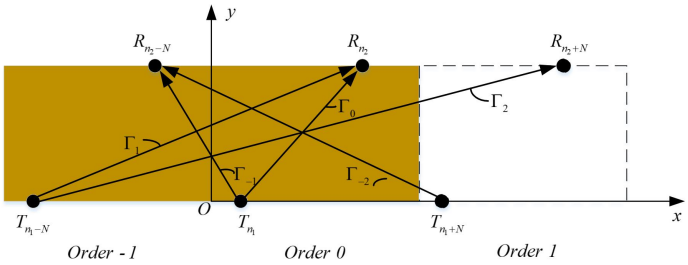

(a)

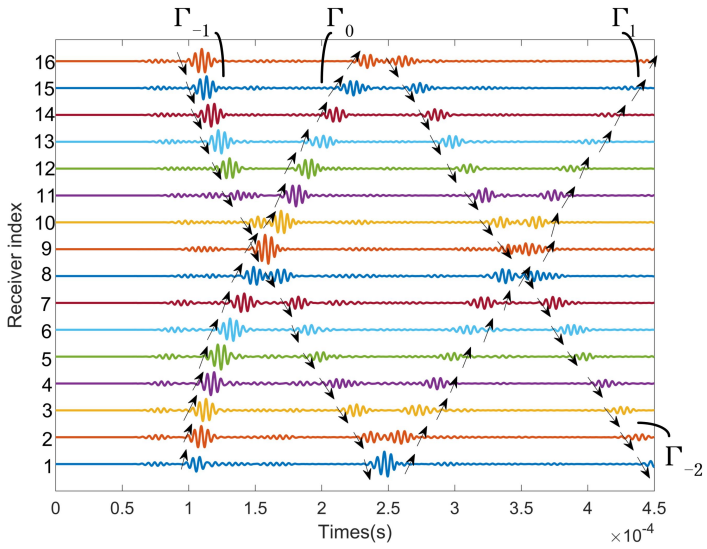

(b)

Fig.12.(a)Helical guided wave paths on the surface *Order -1*, *Order 0 and Order 1*. (b)Waveforms measured across the transducers of the receive array when source #1 radiates. The waveform contains two modes, S0 and A0 mode. The arrows mark the waveforms of the four helical guided waves and the S0 mode is neglected.

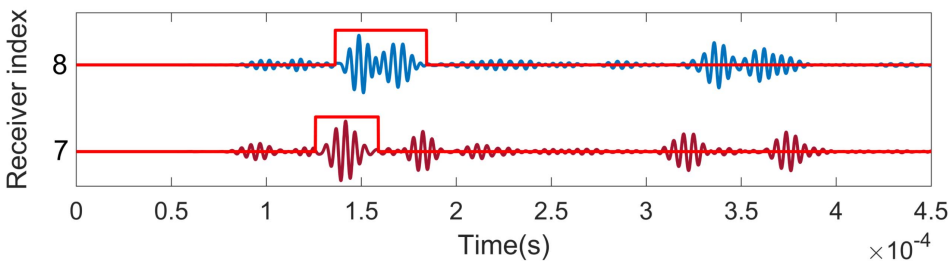

Fig.13. The simple extraction method of useful signals received from transducers #7

and #8.

These two signals in Fig.13 are taken from Fig.12(b). The direct wave signal of probe #7 can be extracted automatically from the original signal with a window function. The overlapped Γ_{-1} and Γ_0 wave from receiver #8 can also take this approach, but their further separation would depend on the method in section 2.2. In particular, the overlapped Γ_{-1} and Γ_0 wave represents two different paths, their travelling distances are 0.425m and 0.489m, respectively, which means the dictionary $\boldsymbol{L}=[\boldsymbol{L}_1,\boldsymbol{L}_2,...,\boldsymbol{L}_r,...,\boldsymbol{L}_R]$ contains only $\boldsymbol{L}_1$ and $\boldsymbol{L}_2$. $\boldsymbol{\phi}$ of this case can be divided as $[0,\pi/50,\pi/25,...,2\pi]$, the phase interval is $\pi/50$. Fig.14 shows the separation results of all signals. The majority of these signals can be extracted by direct interception, and the few signals with serious overlap are selected by constructing dictionaries after removing the S0 modes. The experimental pipeline has rust marks and exhibits slight anisotropy. There is a certain amount of discrepancy between the actual propagation signal and the simulation.

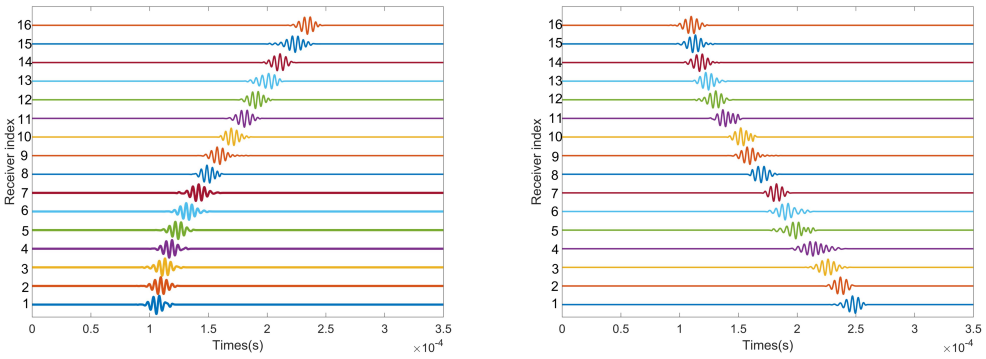

(a) (b)

Fig.14. The received signals after separation. (a) the signals of Γ_0 from the receiving array; (b)the signals of Γ_{-1} from the receiving array.

4.3 Experimental reconstruction

The inversion algorithm similar to the numerical model can be operated to conduct the experimental thickness mapping when all the signals have been separated. Fig.15 demonstrates that this tomography method is also applicable to real environments. The imaging accuracy improves when the acquired signal is sufficiently utilized, i.e., more different order helical guided waves are considered. However, compared to the simulation, the thickness reconstruction of the experimental signal is slightly poor. The defect shape (Fig.15a) is very irregular when the input scattered field data is not sufficient. Fig.16 and Fig.17 show the trend of the thickness variation in a line chosen across the centre of the defect. It can be clearly seen that the thickness gradient varies largely in the defect area of the experimental imaging. The minimum value of the thickness can also provide a certain indication of the corrosion status in the pipe wall. In addition, the experimental results can precisely give the corrosion size and location, and this is instructive for industrial non-destructive testing.

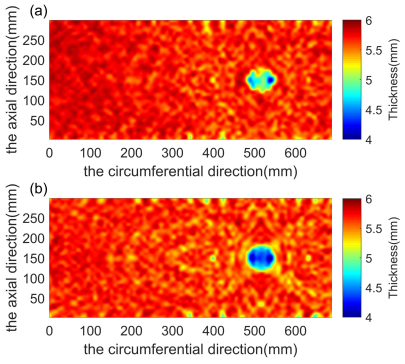

Fig.15. Thickness distribution of the pipe wall employing experiments. (a) The thickness imaging only considering the direct paths; (c) The thickness imaging considering the direct and helical paths.

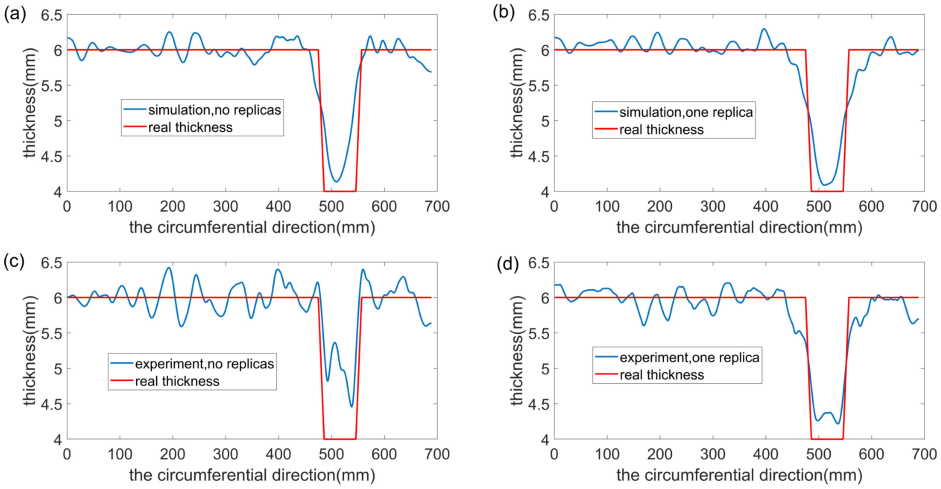

Fig.16. The thickness distribution through the centre of the defect along the circumferential direction. The red lines in the 4 figures represent the true values. (a) The blue line is the simulation result only considering the direct wave paths; (b) The blue line is the simulation result using the helical waves of Γ_{-1}, Γ_0 and Γ_1; (c) The blue line is the experimental result only considering the direct wave paths; (d) The blue line is the experimental result using the helical waves of Γ_{-1}, Γ_0 and Γ_1.

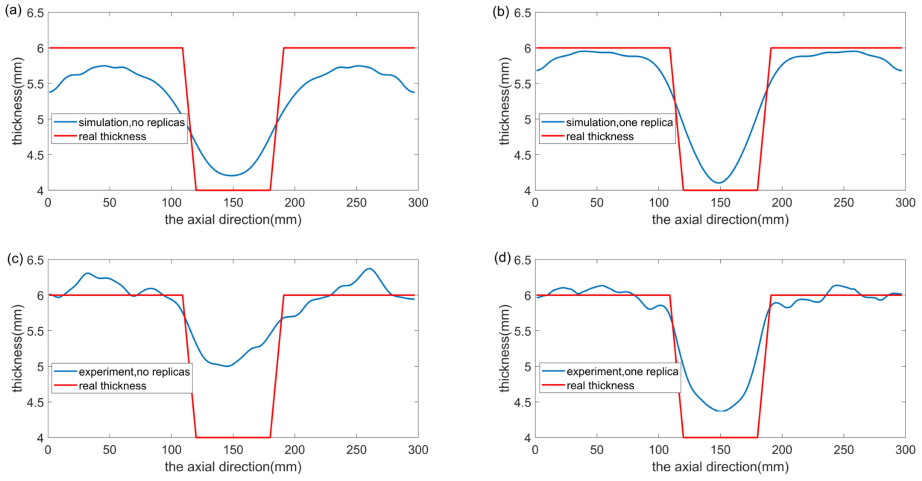

Fig.17. The thickness distribution through the centre of the defect along the axial direction. The red lines in the 4 figures represent the true values. (a) The blue line is the

simulation result only considering the direct wave paths; (b) The blue line is the simulation result using the helical waves of Γ_{-1}, Γ_0 and Γ_1; (c) The blue line is the experimental result only considering the direct wave paths; (d) The blue line is the experimental result using the helical waves of Γ_{-1}, Γ_0 and Γ_1.

In order to provide a more quantitative description of the relationship between the reconstruction results and the actual thickness error, a metric R_{NL} is defined here.

$$R_{NL} = 1 - \sqrt{[\sum_i (T_{exa}^i - T_{cal}^i)^2] / \sum_i (T_{exa}^i)^2} \tag{17}$$

Where: T_{cal}^i represents the thickness value assigned to a reconstructed point *i* within the cross-section, while T_{exa}^i denotes the actual thickness. A smaller reconstruction error is observed when R_{NL} approaches 1, suggesting that the reconstruction of the defect becomes more feasible. The circumferential and axial directions of the pipe wall are defined as the *x* and *y* axes, respectively. When considering only one unfolded surface, replica=0, and when considering two unfolded surfaces, replica=1, and so forth. The calculation results for R_{NL} are provided in Table 2. Through the definition of this parameter, it is evident that higher-order helical guided waves indeed enhance the reconstruction performance of thickness. The improvement of R_{NL} in the experiment is more pronounced although the experimental reconstruction errors are relatively larger compared to simulations.

Table 2

The metric R_{NL} calculated from the simulation and experiment.

R_{NL}	Simulation	Experiment
y=150, replica=0	0.9567	0.9354
y=150, replica=1	0.9628	0.9626
x=516, replica=0	0.9149	0.8969
x=516, replica=1	0.9448	0.9404

5. Discussion

The qualitative conclusions drawn from the experiments and simulations in verifying the algorithms in this paper are consistent. The utilization of high-order helical guided waves can achieve more precise imaging. However, the inversion part of the imaging algorithm relies on the Born approximation in the initial iteration. In the case of more complex defects, the restrictions of this approximation will grow stronger. Therefore, this issue will be discussed in this section at first.

As the pipe wall corrodes very slowly, according to the testing experience of this paper, the wall thickness reduction of 1mm takes about 18 days using hydrochloric acid (20%). Simulation is a reasonable alternative means through the preceding analysis. Fig.18 gives the reconstructed results for two circular defects, their theoretical residual thicknesses are 3mm and 4mm, respectively. When only the direct path signal is considered, the outline of defects with lighter corrosion is extremely ambiguous. The

defect situation in Fig.19 is more complicated, containing three defects of different shapes and depths. The theoretical remaining thickness of defects 1,2 and 3 are 2mm, 3mm and 4mm respectively. Currently, the thickness reconstruction has major errors with the sparse input data. Further detailed quantitative analysis of the thickness is shown in Figs.20 and 21. Fig.20 shows the trend of the thickness variation in a line chosen across the centre of the defect, and Fig. 21 is an error statistic for the double-defect and triple-defect models. The thickness error of both double-defect and triple-defect models can be controlled within 1mm as long as the propagation characteristics of helical guided waves are properly utilized. As shown in Figs.19 and 20, in the model with three defects, the imaging performance did not show a significant improvement at replica=2. When replica changes from 1 to 2, the reconstruction of defect 1 indeed became more accurate, but there was no improvement in the reconstruction of defect 3. On one hand, under the limitations of the Born approximation, the initial solution for the three-defect model is inaccurate, leading to poorer reconstruction results compared to the two-defect model. Furthermore, in the case of multiple defects, high-order helical guided waves experience more severe attenuation and are highly susceptible to noise contamination.

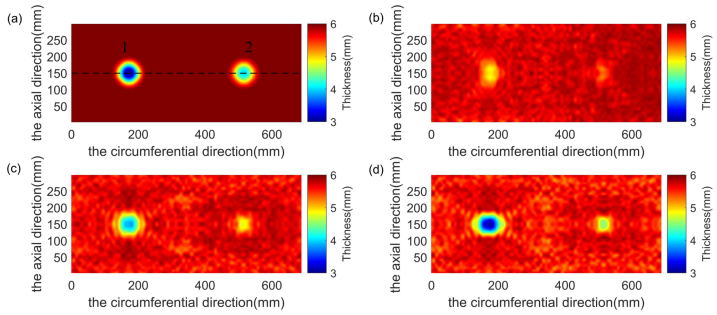

Fig.18. The reconstructed results contain two defects using the simulated data. (a) The theoretical thickness distribution; (b) Wall thickness reconstruction only considering the direct wave paths; (c) Wall thickness reconstruction utilizing all the helical guided waves in the pipe wall of *Order -1* and *Order 0*; (d) Wall thickness reconstruction utilizing all the helical guided waves in the pipe wall of *Order -1* , *Order 0* and *Order 1*.

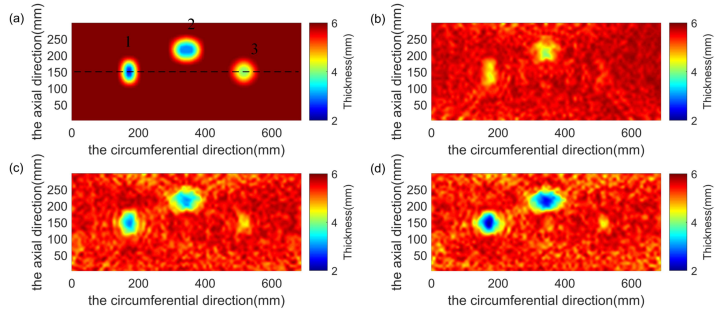

Fig.19. The reconstructed results contain three defects using the simulated data. (a) The theoretical thickness distribution; (b) Wall thickness reconstruction only considering the direct wave paths; (c) Wall thickness reconstruction utilizing all the helical guided waves in the pipe wall of *Order -1* and *Order 0*; (d) Wall thickness reconstruction utilizing all the helical guided waves in the pipe wall of *Order -1* , *Order 0* and *Order 1*.

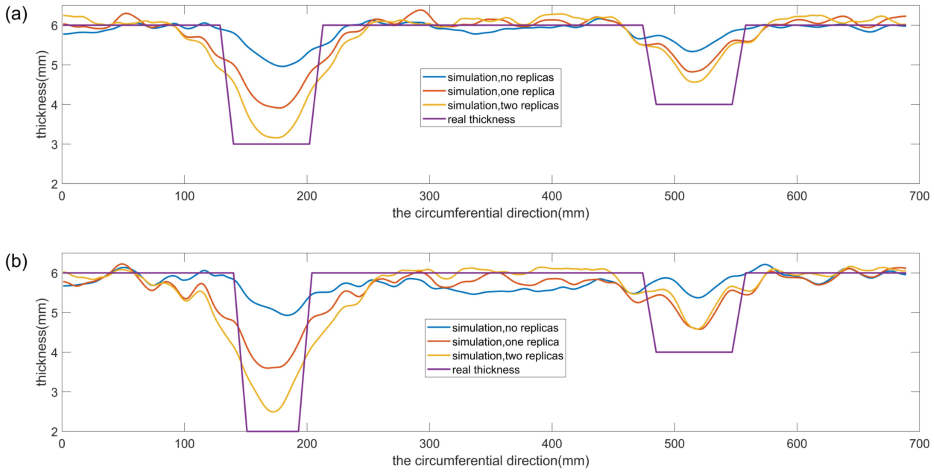

Fig.20. The thickness distribution in a line through the centre of the defect. The purple lines in the 2 figures represent the true values. The other three different colored lines respectively consider different orders of helical wave propagation. (a) The thickness results calculated from Fig.19; (b) The thickness results calculated from Fig.20.

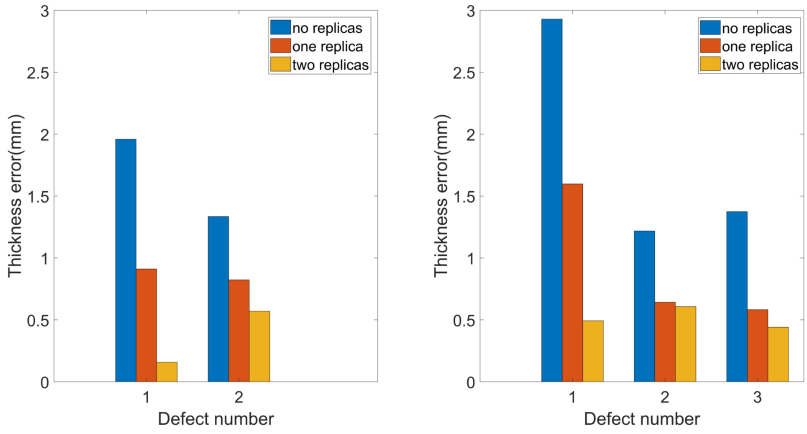

Fig.21. Error analysis of imaging results. (a) Thickness error calculated from Fig.18, including three cases of helical guided waves; (b) Thickness error calculated from Fig.19, including three cases of helical guided waves.

The examples provided in Fig.18 and Fig.19 only considered the damage located strictly between the arrays of transducers and sensors. The corrosion defects in Fig.22

located close to the sensor array have been studied to validate the algorithm's performance. The remaining thicknesses of defects 1 and 2 are 3mm and 4mm, respectively. In this case, the difficulty of signal processing does not increase because the extraction of the scattering field is obtained by subtraction between the healthy and the defective signal. When considering only direct wave signals, thinner defects are almost impossible to observe. This is because fewer rays are passing through the array's edges, making it difficult to clearly describe the characteristics of the defect. When considering helical waves, with a more abundant dataset, it is possible to improve the resolution of defects. The thickness distribution between the centres of the two defects is shown in Fig. 23. It can be easily observed that when more rays pass through the defect, the thickness assessment becomes more accurate.

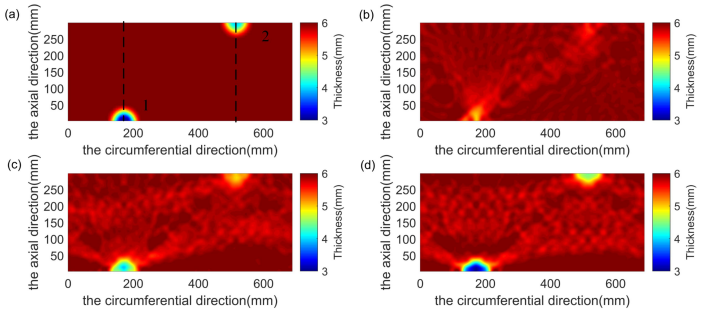

Fig.22. The reconstructed results consider the defects close to the sensor array using the simulated data. (a) The theoretical thickness distribution; (b) Wall thickness reconstruction only considering the direct wave paths; (c) Wall thickness reconstruction utilizing all the helical guided waves in the pipe wall of *Order -1* and *Order 0*; (d) Wall thickness reconstruction utilizing all the helical guided waves in the pipe wall of *Order -1* , *Order 0* and *Order 1*.

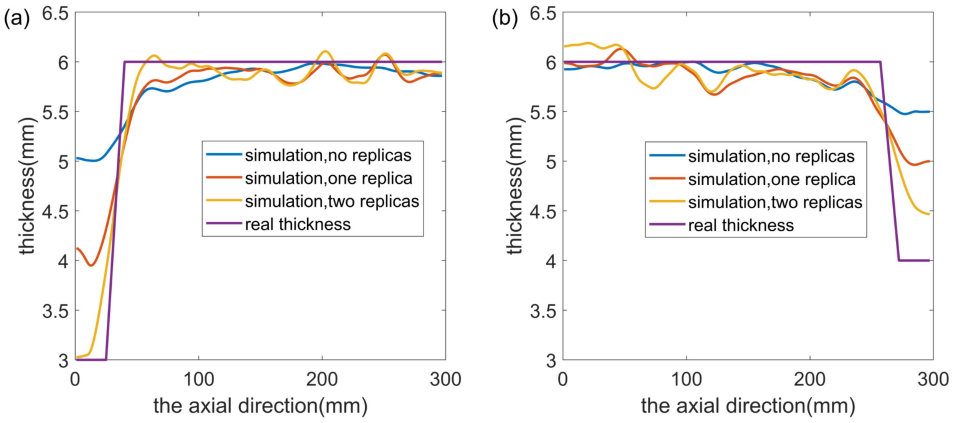

Fig.23. The thickness distribution in a line through the centre of the defect. The purple lines in the 2 figures represent the true values. The other three different colored lines respectively consider different orders of helical wave propagation. (a) The thickness results calculated from defect 1 in Fig.22; (b) The thickness results calculated from defect 2 in Fig.22.

When considering the parameter R_{NL}, a quantitative description of the thickness distribution along the intercepted sections passing through the defect centers in Figs. 18, 19, and 22 are presented in Fig.24. y=150 represents a line segment passing through the defect center in the circumferential direction. Similarly, x=172 and x=516 both correspond to line segments passing through the defect center in the axial direction. As the expansion of the pipe wall surfaces increases, R_{NL} gradually increases and approaches 1. In Fig.24(a), the R_{NL} values for the blue line are significantly better than those for the red line. This is because in more complex defect scenarios, the limitations of the Born approximation are more pronounced, leading to a decrease in the reconstruction accuracy of this algorithm. This phenomenon is also evident in Fig.24(b).

When defects are located near the array, their influence on the reconstruction results is not significant. This is because the defect area in Fig.22 is smaller than that in Fig.18, resulting in only minor phase variations in the waves, which have a smaller impact on the Born approximation.

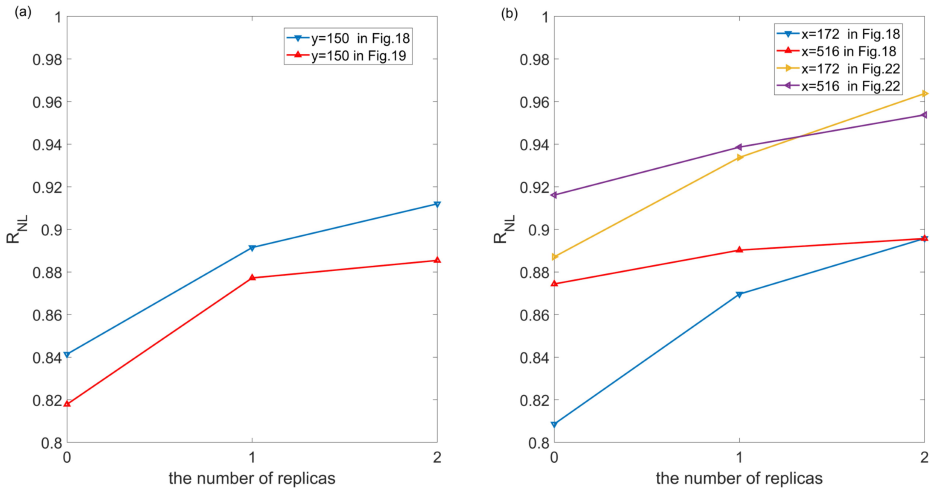

Fig.24. The variations in R_{NL} from different simulation scenarios. (a) The results of R_{NL} calculated from the line along the circumferential direction in Figs.18 and 19; (b) The results of R_{NL} calculated from the line along the axial direction in Figs.18 and 22.

In spite of the iterative idea introduced in this work, the restriction of born approximation remains as well. Besides the born approximation factor, the pipe itself is curved and not equivalent to the plate. The accurate governing equation of the helical guided waves relies on the three-dimensional Lamè–Navier equation, but it is extremely tough to solve and verify experimentally [15]. Therefore, reasonable assumptions in this paper are necessary. Compared to previous work, this paper offers significant improvements as well. In signal processing, a novel method has been proposed to

separate overlapped guided waves. The key point of this method is to minimize the residuals between the reconstructed signal and the original signal by building the path and phase dictionaries. As seen from the experimental signal in Fig.12, the dispersion of signals can worsen the overlap problems, which brings out the necessity of this approach. The restriction of this technique holds that it is only applicable to isotropic structures and the specific propagation path must be known. In terms of defect reconstruction, this paper built the relationship between thickness and objective function directly. The vast majority of imaging algorithms are merely capable of localizing simple defects [13,14,17-19]. Diffraction tomography [20] could also implement thickness mapping, while it requires the same structure with a known defect depth as a reference. The full-waveform inversion [24-26] can obtain the thickness distribution with high precision by iterating over the velocity field. However, the inversion process in this approach is very time-consuming. The convergence for a single frequency can be achieved in 20 to 40 iterations. In the former paper [24], an irregularly shaped defect took around 4.5 hours to get the results. The distorted born iteration method in this work calculates much faster. Take Fig.19(d) as an example, the whole process iterates 8 times, taking 4 minutes for each iteration. Because the dimensionality of the matrix to be solved itself is poor, the detection region is divided into 3306 points and the input scattering field is 2401 in total. Due to the weakness of the full waveform inversion, its application is more often in seismic wave surveys. The methods in this paper can provide some guidance for nondestructive testing and structural health monitoring.

In order to improve the imaging accuracy of complex defects, we can borrow the advantages of HARBUT [21-23] and full waveform inversion. HARBUT selects bent ray tomography to provide the initial solution, overcoming the limitations of the Born approximation. The velocity map obtained in the final iteration at each frequency was used as a starting model for the next frequency in the full waveform inversion. With the application of these two methods, the present algorithm is expected to achieve better results in the future.

6. Conclusion

In this work, a systematic tomography framework containing signal separation and imaging has been presented to enable guided waves propagating in helical paths in the pipe to conduct the thickness mapping. The over-completed dictionary is designed to extract the single wave packet along different paths, so that the scattered field of the single path can be obtained as the input of the imaging algorithm. For reconstructing the pipe defects, the forward governing equation derived from the Helmholtz equation and the inversion model based on the distorted born iteration method are utilized to achieve the objective function, which can be converted to the thickness distribution eventually. Corresponding numerical simulations are carried out, with experimental verification conducted. The conclusions of this study can be summarized as follows:

(1) The helical guided wave travelling on the pipe with a known distance can be separated from the overlapped signals based on the dictionary reconstruction. In particular, this technique appears more essential in experimental signals with dispersion

effects causing the worse distinguishment.

(2) The thickness mapping of the pipe wall can be successfully realized from perspectives of numerical simulations and experimental measurements when the objective function is solved in the distorted born iteration method and converted to thickness.

(3) The algorithm in this paper is superior in high-quality and rapid imaging, while the resolution will drop if the initial objective function is not provided when dealing with complex defect problems.

This work is an attempt to conduct guided wave tomography in isotropic plate-like structures. Not limited by guided waves, it is foreseeable that this imaging method is still suitable for seismic wave inversion and breast ultrasonography since they meet the same acoustic governing equation. Actually, the frequency and bandwidth of seismic and body waves are quite distinct from those of guided waves. The outcome of imaging is uncertain and needs to be explored in the future.

Acknowledgements

The authors gratefully acknowledge the support of the Natural Science Foundation of China (12061131013, 12172171, and 11972276), the State Key Laboratory of Mechanics and Control of Mechanical Structures at NUAA (No. MCMS-I-0522G01), National Natural Science Foundation of Jiangsu Province (BK20211176), Jiangsu High-Level Innovative and Entrepreneurial Talents Introduction Plan (Shuangchuang Doctor Program, JSSCBS20210166), the Fundamental Research Funds for the Central

Universities (NS2022011 and NE2020002), China-UK international cooperation project (12211530064) and a project Funded by the Priority Academic Program Development of Jiangsu Higher Education Institutions (PAPD). Prof. Iren E Kuznetsova thanks Russian Ministry of Science and Higher Education (government task FFWZ-2022-0002) for partial financial support.

References

[1] Cawley P, Lowe MJS, Alleyne DN, Pavlakovic B, Wilcox P. Practical long range guided wave testing: Applications to pipes and rail. Materials evaluation. 2003;61:66-74.

[2] Lowe MJS, Alleyne DN, Cawley P, Pavlakovic B. Rapid, Long Range Inspection of Chemical Plant Pipework Using Guided Waves. Advances in nondestructive evaluation, PT 1-3. 2004;270-273:434-441.

[3] Rose JL. A Baseline and Vision of Ultrasonic Guided Wave Inspection Potential. Journal of pressure vessel technology. 2002;124:273-282.

[4] Brath AJ, Simonetti F, Nagy PB, Instanes G. Guided Wave Tomography of Pipe Bends. IEEE transactions on ultrasonics, ferroelectrics, and frequency control. 2017;64:847-858.

[5] Willey CL, Simonetti F, Nagy PB, Instanes G. Guided wave tomography of pipes with highorder helical modes. NDT & E international : independent nondestructive testing and evaluation. 2014;65:8-21.

[6] Dehghan-Niri E, Salamone S. A multi-helical ultrasonic imaging approach for the

structural health monitoring of cylindrical structures. Structural health monitoring. 2015;14:73-85

[7] Huthwaite P, Seher M. Robust helical path separation for thickness mapping of pipes by guided wave tomography. IEEE transactions on ultrasonics, ferroelectrics, and frequency control. 2015;62:927-938.

[8] Xu C, Yang Z, Chen X, Tian S, Xie Y. A guided wave dispersion compensation method based on compressed sensing. Mechanical systems and signal processing. 2018;103:89- 104.

[9] Jia H, Zhang Z, Liu H, Dai F, Liu Y, Leng J. An approach based on expectation-maximization algorithm for parameter estimation of Lamb wave signals. Mechanical systems and signal processing. 2019;120:341-355.

[10] Jenot F, Ouaftouh M, Duquennoy M, Ourak M. Corrosion thickness gauging in plates using Lamb wave group velocity measurements. Measurement science & technology. 2001;12:1287-1293.

[11] Michaels JE, Lee SJ, Hall JS, Michaels TE. Multi-mode and multi-frequency guided wave imaging via chirp excitations. Proceedings of SPIE - The International Society for Optical Engineering. Bellingham WA: SPIE; 2011;7984.

[12] Livadiotis S, Ebrahimkhanlou A, Salamone S. Monitoring internal corrosion in steel pipelines: a two-step helical guided wave approach for localization and quantification. Structural health monitoring. 2021;20:2694-2707.

[13] Bao Q, Yuan S, Wang Y, Qiu L. Anisotropy compensated MUSIC algorithm based composite structure damage imaging method. Composite structures. 2019;214:293-303.

[14] Liu Z, Sun K, Song G, He C, Wu B. Damage localization in aluminum plate with compact rectangular phased piezoelectric transducer array. Mechanical systems and signal processing. 2016;70-71:625-636.

[15] Brath AJ, Simonetti F, Nagy PB, Instanes G. Acoustic formulation of elastic guided wave propagation and scattering in curved tubular structures. IEEE transactions on ultrasonics, ferroelectrics, and frequency control. 2014;61:815-829.

[16] Keulen CJ, Yildiz M, Suleman A. Damage Detection of Composite Plates by Lamb Wave Ultrasonic Tomography with a Sparse Hexagonal Network Using Damage Progression Trends. Shock and vibration. 2014;2014:1-8.

[17] Kannusamy M, Kapuria S, Sasmal S. An efficient Lamb wave-based virtual refined timereversal method for damage localization in plates using broadband measurements. Ultrasonics. 2022;124:106767-106767.

[18] Zhu N, Jiang Y, Kato S. Ultrasonic computerized tomography (CT) for temperature measurements with limited projection data based on extrapolated filtered back projection (FBP) method. Energy (Oxford). 2005;30:509-522.

[19] Qu H, Xu F, Hu X, Wang L, Zhao J, Zhang Z. A novel denoising method based on Radon transform and filtered back-projection reconstruction algorithm. Optics and lasers in engineering. 2012;50:593-598.

[20] Belanger P, Cawley P, Simonetti F. Guided wave diffraction tomography within the born approximation. IEEE transactions on ultrasonics, ferroelectrics, and frequency control. 2010;57:1405-1418.

[21] Huthwaite P. Guided wave tomography with an improved scattering model.

Proceedings of the Royal Society. A, Mathematical, physical, and engineering sciences. 2016;472:20160643-20160643.

[22] Huthwaite P. Improving accuracy through density correction in guided wave tomography. Proceedings of the Royal Society. A, Mathematical, physical, and engineering sciences. 2016;472:20150832-20150832.

[23] Huthwaite P, Simonetti F. High-resolution imaging without iteration: A fast and robust method for breast ultrasound tomography. The Journal of the Acoustical Society of America. 2011;130:1721-1734.

[24] Rao J, Ratassepp M, Fan Z. Guided Wave Tomography Based on Full Waveform Inversion. IEEE transactions on ultrasonics, ferroelectrics, and frequency control. 2016;63:737-745.

[25] Rao J, Ratassepp M, Lisevych D, Caffoor MH, Fan Z. On-line corrosion monitoring of plate structures based on guided wave tomography using piezoelectric sensors. Sensors (Basel, Switzerland). 2017;17:2882.

[26] Hu Y, Han L, Xu Z, Zhang T. Demodulation envelope multi-scale full waveform inversion based on precise seismic source function. Acta geophysica Sinica. 2017;60:1088-1105.

[27] Volker A. Guided wave tomography in anisotropic media using recursive extrapolation operators. AIP Conference Proceedings. 2018;1949.

[28] Qian Z, Wang B, Zhang Y, et al. Guided Wave Tomography of Surface Defects Based on the Method of Moments. Advanced theory and simulations. 2023;6:n/a.

[29] Qian Z, Li P, Wang B, et al. A novel wave tomography method for defect

reconstruction with various arrays. Structural health monitoring. 2023:147592172311622.

[30] Instanes G, Pedersen A, Toppe M, Nagy PB. Constant group velocity ultrasonic guided wave inspection for corrosion and erosion monitoring in pipes. AIP Conference Proceedings. 2009;1096:1386-1393.

[31] Carandente R, Cawley P. The effect of complex defect profiles on the reflection of the fundamental torsional mode in pipes. NDT & E international : independent nondestructive testing and evaluation. 2012;46:41-47.

[32] Nagy PB, Simonetti F, Instanes G. Corrosion and erosion monitoring in plates and pipes using constant group velocity Lamb wave inspection. Ultrasonics. 2014;54:1832-1841.

[33] Rose J L .Ultrasonic Guided Waves in Solid Media. 2014; Cambridge: Cambridge University Press.

[34] Morse PM, Ingard KU. Theoretical acoustics.1987; *Princeton University Press*.

[35] Kak AC, Slaney M, Wang G. Principles of Computerized Tomographic Imaging. Medical Physics. American Association of Physicists in Medicine. 2002;29:107-107.

[36] Qian Z, Zhang C, Li P, et al. A dictionary-reconstruction approach for separating helical-guided waves in cylindrical pipes. Journal of physics. D, Applied physics. 2023;56:305301.

[37] Xu C, Yang Z, Qiao B, Chen X. A parameter estimation based sparse representation approach for mode separation and dispersion compensation of Lamb waves in isotropic plate. Smart materials and structures. 2020;29:35020.

[38] Liu L, Yuan FG. A Linear Mapping Technique for Dispersion Removal of Lamb Waves. Structural health monitoring. 2010;9:75-86.

[39] Chew W, Wang Y. Reconstruction of 2-dimensional permittivity distribution using the distorted born iterative method. IEEE Transactions On Medical Imaging. 1990;9:218-225.

[40] Haddadin OS, Ebbini ES. Self-focusing arrays for imaging and therapy through inhomogeneous media. 1996 IEEE Ultrasonics Symposium. Proceedings. IEEE; 1996;2:1563-1566.

[41] Liu GR, Quek Jerry SS. A non-reflecting boundary for analyzing wave propagation using the finite element method. Finite elements in analysis and design. 2003;39:403-417.

[42] Moreau L, Castaings M. The use of an orthogonality relation for reducing the size of finite element models for 3D guided waves scattering problems. Ultrasonics. 2008;48:357-366.

[43] Castaings M, Bacon C. Finite element modeling of torsional wave modes along pipes with absorbing materials. The Journal of the Acoustical Society of America. 2006;119:3741-3751.